

Equivalence of elastic and Ising models for spin crossover materials

Gian Ruzzi,* Jace Cruddas, Ross H. McKenzie, and Ben J. Powell

School of Mathematics and Physics, The University of Queensland, QLD 4071, Australia

Spin crossover (SCO) materials are reversible molecular switches; and occur in a wide range of near octahedral transition metal complexes and frameworks with $d^4 - d^7$ electron configurations. SCO systems present collective spin-state phase transitions that show hysteresis, multistep transitions, gradual transitions, and anti-ferroelastic phases. Ising models have often been employed to model these behaviors, as they are far easier to solve than more realistic elastic models. However previously Ising models have required phenomenological parameters that do not have a clear physical origin. We present an exact mapping from an elastic model of balls and springs to the Ising model. The resulting Ising coupling constants arise only from the elastic interactions, and are independent of the lattice dynamics, i.e., there are no isotope effects. The elastic interactions, and hence the Ising coupling constants can be determined from the measurements of the bulk and shear moduli. The Ising coupling constants can be frustrated, their signs can be negative or positive, and their magnitude agrees well with previous estimates from fits of experimental spin-transition curves. The Ising coupling constants follow a power law for large separations between metal centers, in particular an inverse square law for the square lattice. For the square lattice with nearest neighbor elastic interactions this model predicts a diverse range of orders including multistep transitions.

I. INTRODUCTION

Spin crossover molecules can exist in two different electronic states, low spin (LS) and high spin (HS), with pronounced differences in geometry, magnetism, and colour. A LS molecule has the minimum number of unpaired electrons possible, a HS molecule has the maximum number of unpaired d -electrons possible. A transition between these states can be induced by a range of physical perturbations, such as temperature [1], light irradiation [2], pressure [3], magnetic fields [4], and electric fields [5]. The SCO phenomenon has been well documented in octahedral transition metal complexes with $d^4 - d^7$ electron configurations [6]. The molecular bistability of these systems has attracted great interest from the nanoscience community, as this phenomenon has potential applications in data storage and display devices [6, 7]. This interest can be evidenced by the fact that since the discovery of thermally induced SCO, several hundreds of SCO complexes have been synthesised and studied [8]. Furthermore, the change in electronic configuration is accompanied by drastic structural (volume, shape) [9], colour [7] and magnetic changes; these characteristics could have potential applications in mechanical nanoscale machines [10], smart pigments, and optical switches [9].

SCO systems have been reported to present collective phenomena including hysteresis, multistep transitions, gradual transitions, and anti-ferroelastic phases [6, 8]. Cooperative interactions between molecules are a key factor in understanding spin-state phase transitions; as a consequence, experimental advances have been accompanied by theoretical investigations aimed at determining the physical origin of this cooperativity. A wide variety of models have been proposed to explain the microscopic

origin of spin-state transitions; Ising-like models, specially the Wajnflasz and Pick (WP) model [11], macroscopic thermodynamical models, and Landau type models, have been extensively used because of their simplicity and generality [6]. However, the origin of their parameters is unclear given the dramatic simplifications they employ. Refs. [6, 8] provide reviews of well-established models of SCO. All of these models have been successful at reproducing some SCO characteristics, like gradual and abrupt SCO transitions, two step transitions, incomplete transitions and hysteretic behaviour [6, 8].

Even though the previously mentioned models have been able to capture many observed phenomena, recent advances in experimental methods underline the necessity of more realistic theoretical approaches [8]. It is believed that the cooperativity between molecules has an elastic origin; this interaction arises from the pronounced volume change (*ca.* 25% in FeN_6 environments [9]) of the SCO molecules upon spin change [8]. This difference in volume leads to elastic strains and local deformations of the system's lattice, which in turn lead to complicated long and short range interactions. Accordingly, it is desirable to have a consistent model with elastic interactions that leads to the emergence of both short and long range interactions.

Models that explicitly take into account structural degrees of freedom have been proposed, the majority of them employ ball and spring modeling. They have been solved via a variety methods including purely Monte Carlo methods [12, 13], purely molecular dynamics methods [14, 15], and a combination of Monte Carlo methods with damped dynamics [16, 17]. These models have been able to show first order and gradual one-step and two-step phase transitions.

Here we present a method, based on a displaced oscillator transformation, to exactly map an elastic system of balls and springs to an Ising model, Fig. 1. We apply this mapping to the square lattice, but the method can readily

* gian.ruzzivillacres@uq.net.au

be applied to other geometries and other elastic models. We show that the Ising coupling constants arise purely from the elastic interactions. Finally, we estimate the parameters of the model from experimental measurements of bulk and shear moduli and show that, for reasonable parameters, multistep transitions naturally occur in this model.

The paper is organized as follows. In Sec. II we define the balls and springs elastic model, we present the mapping from an elastic model to an Ising model using a square lattice as an example, and we show the purely elastic origin of the Ising coupling constants. In Sec. III we describe the short and long range behavior of the Ising coupling constants. We show that they can be frustrated; that their signs change for different ratios of the elastic constants for stretching and bends, which correspond macroscopically to different ratios of the bulk and shear moduli; and that, for large separations of the metal ions, they decay following a power law. In Sec. IV we provide estimates for the Ising coupling constants based on common bulk and shear moduli of MOFs and SCO complexes, and we compare their magnitudes with estimates of Ising parameters from fits of experimental spin-transition curves. In Sec. V we present Monte Carlo simulations that show a variety of spin-state transitions and orderings even though the model contains only three dimensionless parameters. In Sec. VI we conclude. In Appendix A we show that the Ising coupling constants are independent of the lattice dynamics and hence that there is no isotope effect.

II. DERIVATION OF ISING COUPLING CONSTANTS

We consider a square lattice in two spatial dimensions, with the arrangement of metals and ligands depicted in Fig. 1; with only nearest neighbours elastic interactions, and a harmonic potential on the angle θ between adjacent metal-ligand bonds, Fig. 1. Even though the following discussion focuses on a square lattice, the method used can be readily extended to other elastic models.

This model is appropriate for modeling the in-plane physics of the $1n02$ family of frameworks [18, 19], with the chemical formula $[M(L')_n(L)_2]$, where M is the SCO active metal, L is the in-plane ligand, L' is the interlayer ligand, and $n = 1$ or 2 for bridging and monodentate ligands respectively. The L' ligand is not explicitly described by this model. A typical member of this family is $[\text{Fe}(\text{azpy})_2(\text{NCS})_2]$, where azpy is *trans*-4,4'-azopyridine [20]. The model can also serve to describe the $1n24$ family of Hoffmann frameworks [19, 21]. These have the generic formula $[M(L')_n\{M'(L)_2\}_2]$, where M' is a non-SCO-active metal. A typical example is $[\text{Fe}(\text{pz})\{\text{Au}(\text{CN})_2\}_2]$, where pz is pyrazine [21]. In this case the ‘ligands’ in the model actually describe the composite $M'(L)_2$ groups.

The Hamiltonian describing this system is

$$H = H_\sigma + K + V, \quad (1)$$

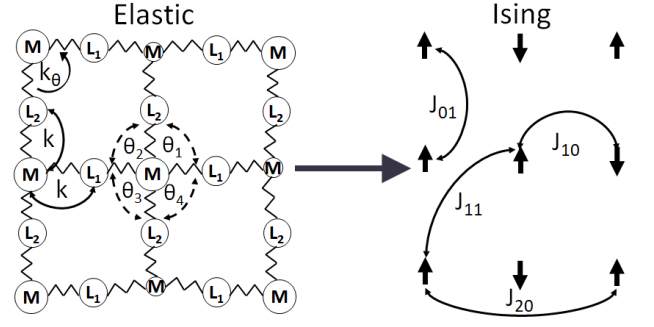


FIG. 1. Mapping from a balls and springs model to an Ising model. (Left) Schematic illustration of a square lattice of metal ions (M) connected to ligands (L_1 , L_2) by springs; smaller circles represent metals in the LS state, and larger circles in the HS state; k is the elastic constant of the springs, and k_θ corresponds to the elastic constant for bending. Each M has four corresponding angle variables θ , see Eq. (1). (Right) Schematic illustration of the corresponding Ising model on a square lattice; the J_{nm} 's are the Ising coupling constants. Up arrows represent a metal in the HS state, and down arrows in the LS state.

where

$$H_\sigma = \frac{1}{2} \sum_{i \in \mathbb{Z}_{N_x}} \sum_{j \in \mathbb{Z}_{N_y}} (\Delta H - T \Delta S) \sigma_{i,j}, \quad (2)$$

$$K = \sum_{i \in \mathbb{Z}_{N_x}} \sum_{j \in \mathbb{Z}_{N_y}} \frac{\mathbf{p}_{M,i,j}^2}{2m_M} + \frac{\mathbf{p}_{L_1,i+\frac{1}{2},j}^2}{2m_{L_1}} + \frac{\mathbf{p}_{L_2,i,j+\frac{1}{2}}^2}{2m_{L_2}}, \quad (3)$$

$$V = \sum_{i \in \mathbb{Z}_{N_x}} \sum_{j \in \mathbb{Z}_{N_y}} \left[\frac{k}{2} \left(|\mathbf{r}_{L_1,i+\frac{1}{2},j} - \mathbf{r}_{M,i,j}| - \bar{R} - \delta\sigma_{i,j} \right)^2 + \frac{k}{2} \left(|\mathbf{r}_{M,i,j} - \mathbf{r}_{L_1,i-\frac{1}{2},j}| - \bar{R} - \delta\sigma_{i,j} \right)^2 + \frac{k}{2} \left(|\mathbf{r}_{L_2,i,j+\frac{1}{2}} - \mathbf{r}_{M,i,j}| - \bar{R} - \delta\sigma_{i,j} \right)^2 + \frac{k}{2} \left(|\mathbf{r}_{M,i,j} - \mathbf{r}_{L_2,i,j-\frac{1}{2}}| - \bar{R} - \delta\sigma_{i,j} \right)^2 + \bar{R}^2 \frac{k_\theta}{2} \sum_{n=1}^4 \sin^2 \left(\frac{\pi}{2} - \theta_{i,j,n} \right) \right]. \quad (4)$$

We have assigned a pseudo-spin variable σ to each metal atom, such that $\sigma = 1$ if the metal is in the high spin (HS) state, and $\sigma = -1$ if it is in the low spin (LS) state. The volume of a SCO molecule decreases when going from the HS state to the LS state, as such the minimum energy metal-ligand separation is dependent on the spin-state of the metal: we set $\bar{R} = (R_{HS} + R_{LS})/2$, $\delta = (R_{HS} - R_{LS})/2$, where R_{HS} (R_{LS}) is the equilibrium distance between the centre of a metal atom in the HS (LS) state and the center of a nearest neighbor ligand. ΔH and ΔS are the enthalpy and entropy difference between the HS and LS states of a single metal center, T is temperature, $\mathbf{r}_{\nu,i,j}$ and $\mathbf{p}_{\nu,i,j}$ are the position and momentum of a group, where $\nu = M, L_1$, or L_2 labels the

species of the group. Note that i and j are both integers for the metals, but one of them is a half-odd-integer for every ligand. m_ν is the mass of species ν , k is the elastic constant of the springs, and $N = N_x \times N_y$, is the number of unit cells.

We define

$$\mathbf{R}_{i,j} = 2i\bar{R}\hat{x} + 2j\bar{R}\hat{y}, \quad (5)$$

$$\mathbf{r}_{\nu,i,j} = \mathbf{R}_{i,j} + \mathbf{u}_{\nu,i,j}. \quad (6)$$

It is important to note that $\mathbf{u}_{\nu,i,j} = (u_{\nu,i,j}^{(x)}, u_{\nu,i,j}^{(y)})$ are displacements about $\mathbf{R}_{i,j}$ rather than the equilibrium positions of the particles. We can think of the lattice formed by $\mathbf{R}_{i,j}$ as an ‘‘average’’ lattice; this construction will simplify our calculations below.

The harmonic approximation, $|\mathbf{u}_{M,i,j} - \mathbf{u}_{L_1,i-\frac{1}{2},j}| \ll \bar{R}$, is implicit in any elastic model. Therefore, without loss of generality

$$\begin{aligned} |\mathbf{r}_{M,i,j} - \mathbf{r}_{L_1,i-\frac{1}{2},j}| &= |\mathbf{u}_{M,i,j} - \mathbf{u}_{L_1,i-\frac{1}{2},j} + \bar{R}\hat{x}| \\ &= u_{M,i,j}^{(x)} - u_{L_1,i-\frac{1}{2},j}^{(x)} + \bar{R}. \end{aligned} \quad (7)$$

Similar results follow for $|\mathbf{u}_{M,i,j} - \mathbf{u}_{L_2,i,j+\frac{1}{2}}|$, $|\mathbf{u}_{L_1,i+\frac{1}{2},j} - \mathbf{u}_{M,i,j}|$, and $|\mathbf{u}_{L_2,i,j+\frac{1}{2}} - \mathbf{u}_{M,i,j}|$. Hence, $V = V_u + V_{u\sigma}$, where

$$\begin{aligned} V_u &= \sum_{i \in \mathbb{Z}_{N_x}} \sum_{j \in \mathbb{Z}_{N_y}} \left[\frac{k}{2} \left(u_{L_1,i+\frac{1}{2},j}^{(x)} - u_{M,i,j}^{(x)} \right)^2 \right. \\ &\quad + \frac{k}{2} \left(u_{M,i,j}^{(x)} - u_{L_1,i-\frac{1}{2},j}^{(x)} \right)^2 + \frac{k}{2} \left(u_{L_2,i,j+\frac{1}{2}}^{(y)} - u_{M,i,j}^{(y)} \right)^2 \\ &\quad + \frac{k}{2} \left(u_{M,i,j}^{(y)} - u_{L_2,i,j-\frac{1}{2}}^{(y)} \right)^2 \\ &\quad + \frac{k\theta}{2} \left(u_{L_2,i,j+\frac{1}{2}}^{(x)} - u_{M,i,j}^{(x)} + u_{L_1,i+\frac{1}{2},j}^{(y)} - u_{M,i,j}^{(y)} \right)^2 \\ &\quad + \frac{k\theta}{2} \left(u_{M,i,j}^{(x)} - u_{L_2,i,j+\frac{1}{2}}^{(x)} + u_{L_1,i-\frac{1}{2},j}^{(y)} - u_{M,i,j}^{(y)} \right)^2 \\ &\quad + \frac{k\theta}{2} \left(u_{L_2,i,j-\frac{1}{2}}^{(x)} - u_{M,i,j}^{(x)} + u_{L_1,i-\frac{1}{2},j}^{(y)} - u_{M,i,j}^{(y)} \right)^2 \\ &\quad \left. + \frac{k\theta}{2} \left(u_{L_2,i,j-\frac{1}{2}}^{(x)} - u_{M,i,j}^{(x)} + u_{M,i,j}^{(y)} - u_{L_1,i+\frac{1}{2},j}^{(y)} \right)^2 \right], \quad (8) \end{aligned}$$

and

$$\begin{aligned} V_{u\sigma} &= \sum_{i \in \mathbb{Z}_{N_x}} \sum_{j \in \mathbb{Z}_{N_y}} \left[u_{L_1,i-\frac{1}{2},j}^{(x)} - u_{L_1,i+\frac{1}{2},j}^{(x)} \right. \\ &\quad \left. + u_{L_2,i,j-\frac{1}{2}}^{(y)} - u_{L_2,i,j+\frac{1}{2}}^{(y)} \right] k\delta\sigma_{i,j}. \end{aligned} \quad (9)$$

Next, we Fourier transform the generalized coordinates of our system, with $\alpha \in \{x, y\}$

$$u_{M,i,j}^{(\alpha)} = \frac{1}{\sqrt{N_x N_y}} \sum_{\mathbf{q}} e^{i\mathbf{q} \cdot \mathbf{R}_{i,j}} u_{M,\mathbf{q}}^{(\alpha)}, \quad (10)$$

$$u_{L_1,i+\frac{1}{2},j}^{(\alpha)} = \frac{1}{\sqrt{N_x N_y}} \sum_{\mathbf{q}} e^{i\mathbf{q} \cdot \mathbf{R}_{i+\frac{1}{2},j}} u_{L_1,\mathbf{q}}^{(\alpha)}, \quad (11)$$

$$u_{L_2,i,j+\frac{1}{2}}^{(\alpha)} = \frac{1}{\sqrt{N_x N_y}} \sum_{\mathbf{q}} e^{i\mathbf{q} \cdot \mathbf{R}_{i,j+\frac{1}{2}}} u_{L_2,\mathbf{q}}^{(\alpha)}. \quad (12)$$

This yields

$$\begin{aligned} K &= \sum_{\mathbf{q}} \left[\frac{\mathbf{p}_{M,\mathbf{q}} \cdot \mathbf{p}_{M,-\mathbf{q}}}{2m_M} + \frac{\mathbf{p}_{L_1,\mathbf{q}} \cdot \mathbf{p}_{L_1,-\mathbf{q}}}{2m_{L_1}} \right. \\ &\quad \left. + \frac{\mathbf{p}_{L_2,\mathbf{q}} \cdot \mathbf{p}_{L_2,-\mathbf{q}}}{2m_{L_2}} \right] \end{aligned} \quad (13)$$

and

$$\begin{aligned} V_u &= \sum_{\mathbf{q}} \left[k u_{L_1,\mathbf{q}}^{(x)} u_{L_1,-\mathbf{q}}^{(x)} - 2k \cos(q_x \bar{R}) u_{M,\mathbf{q}}^{(x)} u_{L_1,-\mathbf{q}}^{(x)} \right. \\ &\quad + (k + 2k\theta) u_{M,\mathbf{q}}^{(x)} u_{M,-\mathbf{q}}^{(x)} + k u_{L_2,\mathbf{q}}^{(y)} u_{L_2,-\mathbf{q}}^{(y)} \\ &\quad - 2k \cos(q_y \bar{R}) u_{M,\mathbf{q}}^{(y)} u_{L_2,-\mathbf{q}}^{(y)} + 2k\theta u_{L_2,\mathbf{q}}^{(x)} u_{L_2,-\mathbf{q}}^{(x)} \\ &\quad + (k + 2k\theta) u_{M,\mathbf{q}}^{(y)} u_{M,-\mathbf{q}}^{(y)} + 2k\theta u_{L_1,\mathbf{q}}^{(y)} u_{L_1,-\mathbf{q}}^{(y)} \\ &\quad - 4k\theta (\cos(q_y \bar{R}) u_{M,\mathbf{q}}^{(x)} u_{L_2,-\mathbf{q}}^{(x)} - \cos(q_x \bar{R}) u_{M,\mathbf{q}}^{(y)} u_{L_1,-\mathbf{q}}^{(y)}) \\ &\quad \left. + \sin(q_x \bar{R}) \sin(q_y \bar{R}) u_{L_2,\mathbf{q}}^{(x)} u_{L_1,-\mathbf{q}}^{(y)} \right] \end{aligned} \quad (14)$$

We rewrite V_u as

$$V_u = \frac{1}{2} \sum_{\mathbf{q}, \alpha, \alpha', \nu, \nu'} \left(f_{\nu, \nu', \mathbf{q}}^{\alpha, \alpha'} u_{\nu, \mathbf{q}}^{(\alpha)} u_{\nu', -\mathbf{q}}^{(\alpha')} \right) \equiv \frac{1}{2} \sum_{\mathbf{q}} \mathbf{u}_{\mathbf{q}}^T \mathbf{F}_{\mathbf{q}} \mathbf{u}_{-\mathbf{q}}, \quad (15)$$

$\mathbf{F}_{\mathbf{q}}$ is the Hessian matrix whose elements are

$$f_{\nu, \nu', \mathbf{q}}^{\alpha, \alpha'} = \frac{\partial^2 V_u}{\partial u_{\nu, \mathbf{q}}^{(\alpha)} \partial u_{\nu', -\mathbf{q}}^{(\alpha')}}. \quad (16)$$

We diagonalize V_u by writing the eigenvalue problem

$$\kappa_{\mathbf{q}} \boldsymbol{\psi}_{\mathbf{q}} = \mathbf{F}_{\mathbf{q}} \boldsymbol{\psi}_{\mathbf{q}}, \quad (17)$$

and find the eigenvalues, $\kappa_{\mathbf{q}}$, and normalized eigenvectors, $\boldsymbol{\psi}_{\mathbf{q}}$, such that

$$\mathbf{u}_{\mathbf{q}}^T \mathbf{F}_{\mathbf{q}} \mathbf{u}_{-\mathbf{q}} = \mathbf{Q}_{\mathbf{q}}^T D_{\mathbf{q}} \mathbf{Q}_{-\mathbf{q}}, \quad (18)$$

where $\mathbf{Q}_{\mathbf{q}} = U_{\mathbf{q}}^T \mathbf{u}_{\mathbf{q}}$, $\mathbf{u}_{\mathbf{q}}$ is a six-dimensional column vector whose components are $u_{\nu, \mathbf{q}}^{(\alpha)}$, $U_{\mathbf{q}}$ is a square matrix whose columns are $\boldsymbol{\psi}_{\mathbf{q}}$, and $D_{\mathbf{q}}$ is a diagonal matrix whose elements are $\kappa_{\mathbf{q}}$. With this transformation $u_{\nu, i, j}^{(\alpha)}$ takes the form

$$u_{\nu, i, j}^{(\alpha)} = \frac{1}{\sqrt{N_x N_y}} \sum_{\mu, \mathbf{q}} e^{i\mathbf{q} \cdot \mathbf{R}_{i,j}} Q_{\mu, \mathbf{q}} \psi_{\nu, \mathbf{q}}^{(\alpha)\mu}, \quad (19)$$

where $\mu = 1, \dots, 6$ enumerates the eigenvalues of the Hessian matrix, $Q_{\mu, \mathbf{q}}$ are the components of the column vector $\mathbf{Q}_{\mathbf{q}}$, and $\psi_{\nu, \mathbf{q}}^{(\alpha)\mu}$ are the components of the orthonormal eigenvectors $\boldsymbol{\psi}_{\mathbf{q}}^{\mu}$. With this change of basis

$$V_u = \frac{1}{2} \sum_{\mu, \mathbf{q}} \kappa_{\mu, \mathbf{q}} Q_{\mu, \mathbf{q}} Q_{\mu, -\mathbf{q}} \quad (20)$$

and

$$V_{u\sigma} = \sum_{\mu, \mathbf{q}} \xi_{\mu}(\mathbf{q}) Q_{\mu, \mathbf{q}} \sigma_{-\mathbf{q}}, \quad (21)$$

where

$$\xi_\mu(\mathbf{q}) = -2i\delta k \left[\psi_{L_1, \mathbf{q}}^{(x)\mu} \sin(q_x \bar{R}) + \psi_{L_2, \mathbf{q}}^{(y)\mu} \sin(q_y \bar{R}) \right], \quad (22)$$

and

$$\sigma_{i,j} = \frac{1}{\sqrt{N_x N_y}} \sum_{\mathbf{q}} e^{i\mathbf{q} \cdot \mathbf{R}_{i,j}} \sigma_{\mathbf{q}}. \quad (23)$$

Now we make a displaced oscillator transformation, which defines

$$v_{\mu, \mathbf{q}} = Q_{\mu, \mathbf{q}} + \frac{\xi_\mu(-\mathbf{q})}{\kappa_{\mu, \mathbf{q}}} \sigma_{\mathbf{q}}. \quad (24)$$

This is essentially ‘‘completing the square’’ so that the interaction between Q and σ is replaced by an interaction between pseudo-spins. The Hamiltonian then takes the form

$$H = H_v + H_\sigma + H_{\sigma\sigma}, \quad (25)$$

where

$$H_v = K + \frac{1}{2} \sum_{\mu, \mathbf{q}} \kappa_{\mu, \mathbf{q}} v_{\mu, \mathbf{q}} v_{\mu, -\mathbf{q}}, \quad (26)$$

and

$$\begin{aligned} H_{\sigma\sigma} &= - \sum_{\mu, \mathbf{q}} \frac{|\xi_\mu(\mathbf{q})|^2}{2\kappa_{\mu, \mathbf{q}}} \sigma_{\mathbf{q}} \sigma_{-\mathbf{q}} \\ &= \sum_{i,j,n,m} J_{n,m} \sigma_{i,j} \sigma_{i+n,j+m}, \end{aligned} \quad (27)$$

where we identify J_{nm} as the Ising coupling constants between sites i, j and $i+n, j+m$,

$$\begin{aligned} J_{n,m} &= - \frac{1}{N_x N_y} \sum_{\mu, \mathbf{q}} \frac{|\xi_\mu(\mathbf{q})|^2}{2\kappa_{\mu, \mathbf{q}}} e^{i\mathbf{q} \cdot (\mathbf{R}_{i,j} - \mathbf{R}_{i+n,j+m})} \\ &= \sum_{\mu} J_{n,m}^{\mu}, \end{aligned} \quad (28)$$

where,

$$J_{n,m}^{\mu} = - \frac{\bar{R}^2}{\pi^2} \int_{BZ} d^2 \mathbf{q} \frac{|\xi_\mu(\mathbf{q})|^2}{2\kappa_{\mu, \mathbf{q}}} \cos [2q_x \bar{R}n + 2q_y \bar{R}m], \quad (29)$$

and the integral over the first Brillouin zone is defined as $\int_{BZ} = \int_{-(\pi/2\bar{R})}^{(\pi/2\bar{R})} \int_{-(\pi/2\bar{R})}^{(\pi/2\bar{R})}$ and in the final equality we have taken the limit $N_x, N_y \rightarrow \infty$.

The final expression for H is

$$\begin{aligned} H &= \frac{1}{2} \sum_{i,j} (\Delta H - T\Delta S) \sigma_{i,j} + \sum_{i,j,n,m} J_{n,m} \sigma_{i,j} \sigma_{i+n,j+m} \\ &\quad + H_v. \end{aligned} \quad (30)$$

As H_v is independent of the $\sigma_{i,j}$ (cf. Eq. 26) this means that the elastic degrees of freedom and the pseudospins are decoupled.

$J_{n,m}$ can be evaluated exactly in a few special cases. If we set $k_\theta = 0$, the eigenvalues and eigenvectors of the Hessian take a simple analytical form, and the Ising coupling constants, between metal sites (i, j) and $(i+n, j+m)$, are given by

$$J_{n,m} = -2k\delta^2 \frac{1}{4\pi^2} \int_{-\pi}^{\pi} \int_{-\pi}^{\pi} d\phi d\phi' \cos[\phi n + \phi' m] = 0, \quad (31)$$

for all $n, m \in \mathbb{Z}$, where $\phi = 2\bar{R}q_x$, $\phi' = 2\bar{R}q_y$.

Similarly, for a one-dimensional chain in one spatial dimension (and therefore with no bending possible), the contributions from the different eigenvalues/eigenvectors of the Hessian matrix cancel each other out, this leads to no Ising interactions between the metal centres. This is because the chain will simply increase or decrease in length to accommodate the metal centres with different spin states. This result is also consistent with the one-dimensional model presented by Boukheddaden, *et al.* [22]; in their model, spin crossover molecules are connected by springs whose elastic constants depend on the spin states of the molecules. In the case where all elastic constants are equal the Ising coupling constants vanish.

Again, the Ising coupling constants of our model vanish for the cubic lattice without angular interactions. This demonstrates that the angular interactions play a key role in collective SCO phenomena.

It is important to note that the origin of the Ising coupling constants is purely from the elastic interactions. They are independent of the mass of the ligands and metals, and do not depend on the dynamics of the system, thus there is no isotope effect; see Appendix A for a detailed discussion.

III. EVALUATION OF THE ISING COUPLING CONSTANTS

For $k_\theta > 0$, the Ising coupling constants are non-zero; however, the eigenvalues/eigenvectors of the Hessian cannot be computed analytically. Therefore we perform the integral numerically, unless otherwise stated we use a 2000×2000 Monkhorst-Pack [23] grid and set $\bar{R} = 49\delta$ (see Sec. IV).

A. Short range behaviour

We report the near neighbor couplings for selected k_θ/k in Fig. 2 and the k_θ/k dependence of selected $J_{n,m}$ in Fig. 3. It is apparent from these data that $J_{1,0}$ is always positive (i.e., anti-ferromagnetic) and $J_{1,1}$ is always negative (i.e., ferromagnetic). However, the signs of many of the other the $J_{n,m}$ change as k_θ/k varies. For example, for small k_θ/k , the $J_{n,0}$ are all positive, but as the ratio approaches unity, they become negative for $n > 1$, only $J_{1,0}$ remains positive.

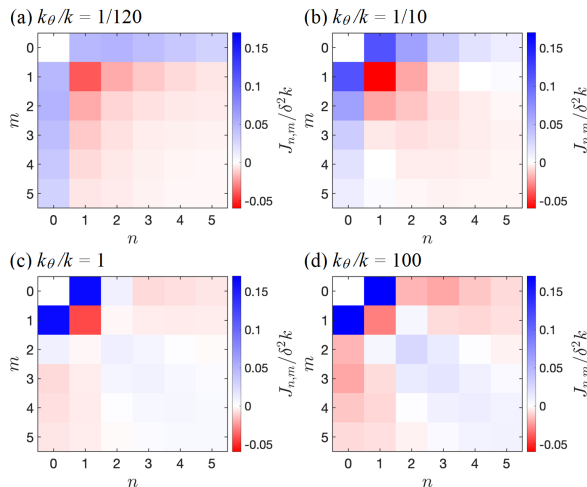


FIG. 2. Short-range spatial dependence of the Ising interactions, for different values of k_θ/k . There is significant frustration for $k_\theta/k \ll 1$, but as k_θ/k increase this is lifted and the near neighbor interactions cooperate to stabilize Néel order.

For large k_θ/k the Ising coupling constants approach constant values. As k_θ/k gets larger, the magnitude of $J_{1,0}$ becomes larger and increases faster than any of the other $J_{n,m}$. Hence, k_θ/k controls the frustration and cooperativity in the system. For example, for $k_\theta/k \ll 1$ (Fig. 2a) the magnitudes of the Ising coupling constants are comparable, which will introduce significant frustration. At $k_\theta/k = 1$ (Fig. 2c) $J_{1,0}$ and $J_{1,1}$ are much larger than the other Ising coupling constants. However, $J_{1,0} > 0$ and $J_{1,1} < 0$ therefore, they cooperate in stabilizing Néel order, which is commonly observed in the $1n02$ [19, 20, 24–27] and $1n24$ [19, 28–35] families. However, the other short-range interactions remain important and other long-range ordered phases may also be stabilized, as we will discuss in Section V. For $k_\theta/k \gg 1$ (Fig. 2d) $J_{1,0}$ has a much larger magnitude than the other $J_{n,m}$. Therefore, the short-range interactions continue to favor Néel order.

Surprisingly, when k_θ/k is sufficiently small, $J_{2,0}$ can be larger than $J_{1,0}$. However, all $J_{n,m}$ vanish as k_θ/k approaches zero, consistent with the analytical result for $k_\theta = 0$, Eq. (31).

Our expression (Eq. (28)) for the Ising couplings consists of a decomposition into different contributions from the six different eigenvectors (elastic modes) of the Hessian matrix (Eq. (16)). One might hope to gain some physical insight from looking at the relative contributions from the different modes and how they vary as the parameter ratio k_θ/k varies. Relevant plots of both the different contributions and the mode dispersion relations are shown in the Supplementary material. It is not possible to make many generalisations about the relative contributions and how they vary with k_θ/k . All modes contribute significantly, except when k_θ/k becomes larger than one, the contributions of modes with the three

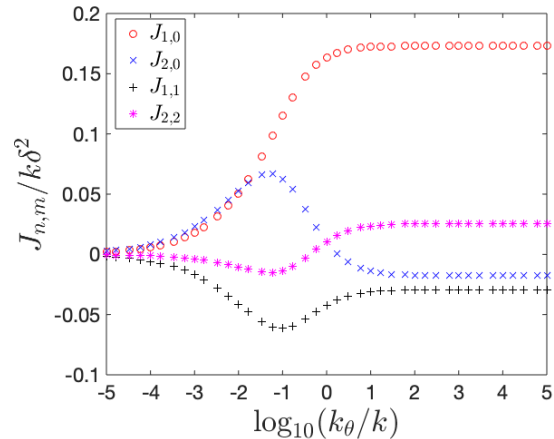


FIG. 3. Dependence of selected Ising couplings on the relative stiffnesses to bending, k_θ , and stretching, k . As k_θ varies, the signs of all the Ising constants other than $J_{1,0}$ and $J_{1,1}$ change. For increasing k_θ , $J_{1,0}$ increases, but the other Ising coupling constants vary non-monotonically. However, for $k_\theta/k > 1$ all the Ising interactions approach constant values. For $k_\theta/k < 0.013$, $J_{2,0}$ is slightly larger than $J_{1,0}$, and as k_θ approaches 0, all Ising couplings vanish, consistent with the analytical result for $k_\theta = 0$, Eq. 31. For $k_\theta/k > 1$, the Ising coupling constants approach constant values. $J_{1,0}$ is always positive and $J_{1,1}$ is always negative, but the signs of $J_{2,0}$ and $J_{2,2}$ depend on k_θ/k .

largest eigenvalues becomes negligible. For all the Ising couplings the relative sign of the contributions from the different modes changes as k_θ/k varies, indicating a subtle competition between the different modes.

B. Long range behaviour

For large separations between metal centers, the Ising coupling constants follow a power law decay. On the square lattice we find an inverse square law: Fig. 4 demonstrates that $|J_{n,0}| = An^{-2}$ and $|J_{n,n}| = Bn^{-2}$ for large n , where A and B are constants that depend on the ratio k_θ/k . This is very different from previous approximate derivations of Ising models for SCO materials, which either only contain short-range interactions [6, 36] or result in infinite range interactions (that are independent of the separation between metal centers) [19, 36–39].

It has recently been proposed that spin-state ices can occur in SCO materials on frustrated lattices [39, 40]. This phase is not characterized by a spontaneously broken symmetry, but rather by a local constraint or ice-rule. On the kagome lattice this dictates that each triangle contains two HS and one LS metals (or *vice versa*). The low energy excitations are fractionalized particles with a spin intermediate between the HS and LS states. Whether or not these quasiparticles are deconfined (and hence whether the spin-state ice exists) depends on the

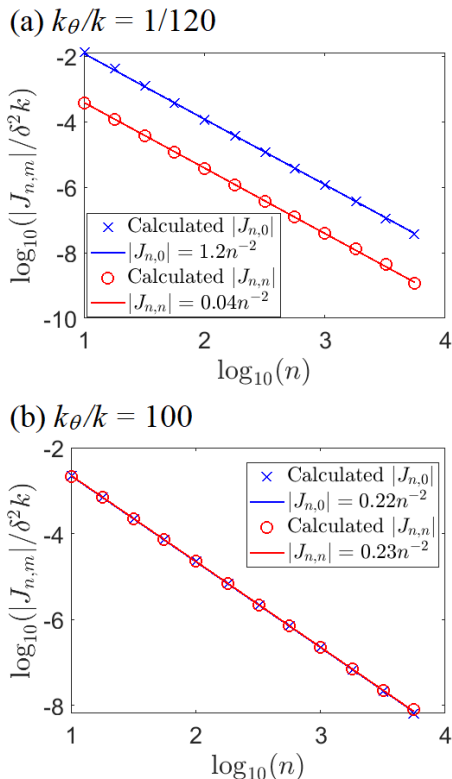


FIG. 4. Logarithmic plots of $|J_{n,0}|$ and $|J_{n,n}|$ as a function of n , displaying power law behaviour for large n , irrespective of the ratio k_{θ}/k . Linear fits were performed using a least-squares method. The Ising coupling constants were calculated using a 50000×50000 grid.

nature of the long-range interactions.

In particular an infinite-range interaction suppresses spin-state ice. Consequently, previous work [39, 40] only finds spin-state ice in regions of parameter space where the infinite-range interaction is very weak. In contrast, long-range interactions that obey an inverse square law do not suppress ice phases [41]. Therefore, our finding that the long-range interactions obey a power law suggest that spin-state ice phases are more stable than has been previously appreciated.

It has also been shown [36–38] that the details of the long-range interaction are crucial for accurately describing the thermodynamics and critical behavior of SCO materials. Therefore, the proper characterization of the long-range interactions is vital for an accurate modeling of experiments.

IV. PARAMETER VALUES

In order to extract values for the spring constants, we can use the the bulk modulus derived for a cubic lattice

with nearest neighbours elastic interactions [42]

$$B = \frac{1}{6}k \left(\frac{N}{V_o} \right)^{1/3}, \quad (32)$$

where N is the total number of unit cells, k is the spring constant between nearest neighbours, and V_o is the volume of the system at equilibrium. Eq. (32) differs by a factor of 1/2 from the expression in [42], because in our case we have two springs between neighboring metal sites. With this expression we can use experimental values to estimate k . For the elastic constant involved in angular interactions, k_{θ} , we can use the shear modulus of a cubic lattice, see Supplementary material,

$$G = \frac{k_{\theta}}{2\bar{R}}, \quad (33)$$

combining with Sec. III A this means that $G \neq 0$ is required for non-zero Ising interactions. For a cubic lattice $V_o/N \approx (2\bar{R})^3$, substituting in Eq. (32)

$$B = \frac{k}{12\bar{R}}, \quad (34)$$

and

$$\frac{k}{k_{\theta}} = 6 \frac{B}{G}. \quad (35)$$

Typical values for these parameters for frameworks and SCO complexes are $B = 4 - 20$ GPa, $G = 0.01 - 4$ GPa, $2\bar{R} = 6 - 10$ Å [43–45].

For \bar{R} we can use experimental data on the distance between metal sites at HS and LS. Typically $2\delta \approx 0.2$ Å for Fe(II) complexes and $2\delta \approx 0.1 - 0.13$ Å for Fe(III) complexes [46].

Using these values we can estimate the magnitude of the Ising coupling constants; here we choose $\bar{R} = 4.9$ Å and $\delta = 0.1$ Å, such that $R_{HS} = 5.0$ Å, and $R_{LS} = 4.8$ Å; $G = 1.0$ GPa, and $B = 4 - 20$ GPa. This yields $J_{10} = 15$ to 40 K, $J_{11} = -10$ to -33 K, and $J_{20} = 11$ to 43 K. Thus, these Ising constants are all of the same order of magnitude. By changing the ratio k_{θ}/k one can make either $J_{10} < J_{20}$ or $J_{10} > J_{20}$. Moreover, $J_{n0} > 0$ for any n , therefore the first few J_{n0} will induce considerable frustration in the system.

Slichter and Drickamer [47] proposed a simple model for the free energy of a SCO system, where the cooperativity of the system is given by the “cooperativity parameter” Γ . Later, Rao, Ganguli, and McGarvey proposed a more general form for the free energy; this free energy model can be compared to an Ising model of the form

$$H = \sum_{i,j} \left[\frac{(\Delta H - T\Delta S)}{2} \sigma_{i,j} - \frac{1}{2} \sum_{n,m} J_{n,m} \sigma_{i,j} \sigma_{i+n,j+m} \right]. \quad (36)$$

in the mean-field approximation [6], such that $J_{n,m}$ and Γ are related via

$$\sum_{n,m} J_{n,m} = \frac{\Gamma}{2N_A}, \quad (37)$$

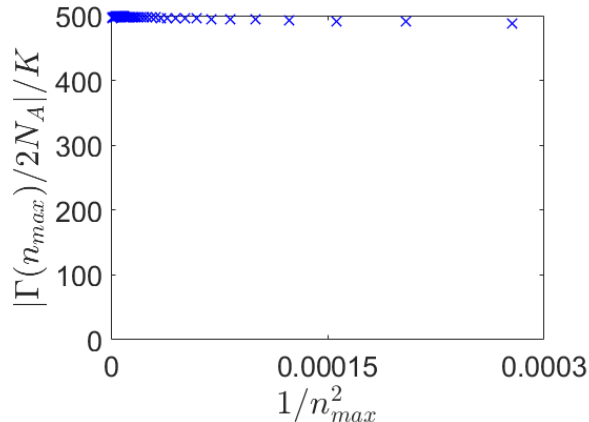


FIG. 5. Cooperativity parameter Γ for different truncation values n_{max} , Eq. (38). As the truncation value increases Γ converges to 490 K. The Ising coupling constants were calculated using a 25000×25000 grid, for $B = 20$ GPa and $G = 4$ GPa.

where N_A is Avogadro's number. Roubeau *et al.* [48] reported values of Γ for a variety of SCO systems. They found that Γ ranges from about 3 to 6 kJ/mol (300 to 750 K).

To numerically evaluate Γ we truncate the sum, and define

$$\Gamma(n_{max}) = 2N_A \sum_n^{n_{max}} \sum_m^{n_{max}} J_{n,m}. \quad (38)$$

For $B = 20$ GPa and $G = 4$ GPa we find $\Gamma(n_{max})/2N_A$ converges to 490 K as $n_{max} \rightarrow \infty$, Fig. 5, which is entirely consistent with the values estimated from fits to experiments by Roubeau *et al.* [48]. Similar results are found for other B and G . Note that previously Γ has often been interpreted in terms of a *nearest neighbor* Ising model, in our case $4J_{1,0} = 277$ K. Thus the four nearest neighbor interactions represent more than half of the value of Γ , this underlines how important the short range interactions are in this model.

V. COLLECTIVE BEHAVIOR

We now show that despite containing just three dimensionless parameters k_θ/k , $\Delta H/k\delta^2$, and $\Delta S/k_B$ our model predicts many of the diverse properties observed in the $1n02$ and $1n24$ SCO frameworks. We performed Monte Carlo (MC) simulations using the Metropolis algorithm, for different combinations of k_θ/k and ΔH ; with $\Delta S = 4 \ln(5)k_B$. The simulations were performed on a 60×60 lattice, using 30 000 MC steps, Figs. 6a and b, and 300 000 MC steps, Fig. 6c, per temperature; each MC step consists of 3600 interrogations of individual metal centres. For the thermodynamic averages we discarded the first third of MC steps. In order to numerically solve this model with a reasonable amount of computational

time, given the power law decay of these constants, we choose a cut-off distance, and set all Ising coupling constants above this cut-off equal to zero. The cut-off for the Ising coupling constants was set to $n_{max} = m_{max} = 10$. The simulations were initialized at $T = 8.52$ K, with all metals in the LS state. The Ising coupling constants were calculated using a 5000×5000 Monkhorst-Pack grid.

In Fig. 6 we plot the thermal dependence of the fraction of HS metals and the heat capacity of the system. We observe a multi-step transition, evidenced by multiple plateaus in the fraction of HS metals and peaks in the specific heat capacity. Each plateau corresponds to a different phase with a different antiferroelastic order, Fig. 7. The number of phases observed at different temperatures depends on ΔH ; for $\Delta H \approx k\delta^2$ we observe a five-step transition, and as $\Delta H/k\delta^2$ increases the number of observed phases decreases, compare Fig. 6a and b. Increasing ΔH also makes the transitions less pronounced (more crossover-like). It has been shown in previous studies of Ising models for SCO material [19] that this is because increasing ΔH moves the system from first order SCO transitions, through a series of critical points, into the crossover regime.

Increasing k_θ/k , compare Figs. 6a and c, also decreases the number of steps, but leaves the transitions relatively sharp. The decrease in the number of phases as k_θ/k increases can be understood from the discussion in Sec. III A. For small k_θ/k many of the Ising coupling constants for near neighbors have comparable magnitudes, cf. Fig. 2. This leads to considerable frustration in the system, which, in turn, leads to multiple competing orders. As k_θ/k increases the magnitude of the nearest neighbor Ising coupling, $J_{1,0}$, becomes significantly larger than other Ising couplings, cf. Fig. 3. This reduces the frustration in the system, which means that fewer phases are observed. The spin-state orders found in the intermediate plateaus, Fig. 7, are consistent with those observed experimentally in the $1n02$ and $1n24$ families of framework materials that our model describes [19]. At $n_{HS} = 1/2$ we find Néel order, Fig. 7d,e, and g, which is the order found in these materials at $n_{HS} = 1/2$ [19, 20, 24–35]. Away from $n_{HS} = 1/2$ the spin-states order in diagonal stripes. Again, this order is found in experiments on these families of materials for $n_{HS} \neq 1/2$ [28, 29, 31–33, 35, 49].

VI. CONCLUSION

We have shown that there is an exact mapping, based on the displaced oscillator transformation, between elastic and Ising models of SCO materials. We have shown this explicitly for a particular model on the square lattice, but our approach can be extended to other elastic models and geometries.

The Ising interactions arise from the elastic potential alone and not from the dynamical behaviors of the

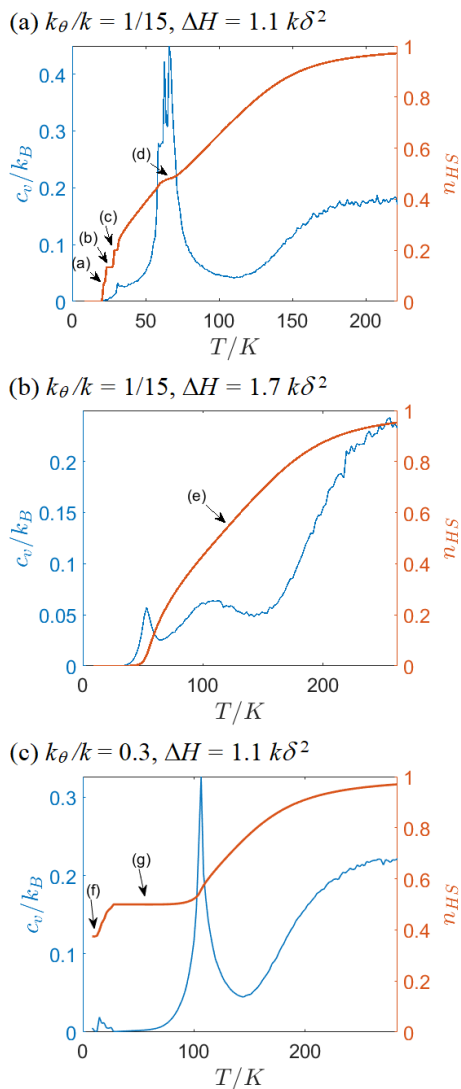


FIG. 6. Heat capacity, c_v , (left axes; blue), and fraction of HS metals, n_{HS} , (right axes; orange), for different k_θ/k and ΔH . (a) For $k_\theta/k \ll 1$ and $\Delta H \approx k\delta^2$ we see a five-step transition. (b) As we increase ΔH and keep $k_\theta/k \ll 1$ the number of steps reduces to two. (c) For larger k_θ/k we observe an incomplete, three-step transition with a broad plateau at $n_{HS} = 0.5$. The arrows marked a-g show the simulations from which the snapshots shown in Fig. 7 were taken.

phonons. This means that there is no isotope effect for SCO. Although our model is purely classical it is straightforward to extend the calculation to a quantum treatment of phonons, yielding precisely the same Ising model as the classical calculation. The quantum treatment might tempt one to ascribe the Ising interaction to the exchange of virtual phonons [50]. This would be incorrect.

The Ising model has both short-range and long-range parts. The degree of frustration in the short-range Ising interactions depends strongly on the relative cost of

bending and stretching, k_θ/k . For large k_θ/k nearest neighbor interactions dominate; there is little frustration and a small number of steps are observed. As k_θ/k decreases the other near neighbor interactions become important and the system becomes frustrated. This leads to multiple competing order parameters and multistep transitions with many steps.

At large distances the Ising interactions follow a power law (inverse square law for the square lattice model investigated in detail). This will have important implications for the emergent physics of SCO materials. For example, previous calculations predicting a spin-state ice used an approximate method to map an elastic model to an Ising model, which resulted in an infinite-range interaction [39, 40]. When this interaction is strong it suppresses the ice phase by confining the fractionalized excitations. Therefore, our exact mapping from elastic models to Ising models suggests that ice phases are more stable than previously expected.

The explicit model we discuss is relevant to the $1n02$ and $1n24$ families of SCO frameworks. It is simple enough to be parameterized from standard experiments (measurements of the bulk and shear moduli, heat capacity, and the crystal structure). Using typical parameters, extracted from these experiments, we find strong agreement with the experimental situation in the $1n02$ and $1n24$ families. In particular, we find prominent multi-step transitions and Néel spin-state order at $n_{HS} = 1/2$ and diagonal stripes at other intermediate plateaus.

ACKNOWLEDGMENTS

This work was supported by the Australian Research Council through grant number DP200100305. We thank Nena Batenburg for helpful discussions and Zejun Huang for helpful comments on a draft of this manuscript.

Appendix A: Independence of the Ising coupling constants from lattice dynamics

The Ising coupling constants arise purely from the interactions between metals and ligands, and do not depend on the dynamics of the system. In particular there is no isotope effect. To see this consider the mass weighted Fourier transform

$$u_{\nu,i}^{(\alpha)}(t) = \frac{1}{\sqrt{N}} \sum_{\mathbf{q}} \frac{1}{\sqrt{m_\nu}} e^{i\mathbf{q}\cdot\mathbf{R}_i} \tilde{u}_{\nu,\mathbf{q}}^{(\alpha)} e^{-i\omega_{\mathbf{q}} t} \quad (\text{A1})$$

where we have made the time dependence of $u_{\nu,i}^{(\alpha)}$ explicit. Using Hamilton's equations of motion on H_u we arrive to the eigenvalue problem

$$\omega_{\mathbf{q}}^2 \tilde{\psi}_{\mathbf{q}} = \mathcal{D}_{\mathbf{q}} \tilde{\psi}_{\mathbf{q}}, \quad (\text{A2})$$

where $\tilde{\psi}_{\mathbf{q}}$ is a column vector whose elements are $\tilde{\psi}_{\nu,\mathbf{q}}^{(\alpha)}$, the dynamical matrix, $\mathcal{D}_{\mathbf{q}}$, is a square matrix whose ele-

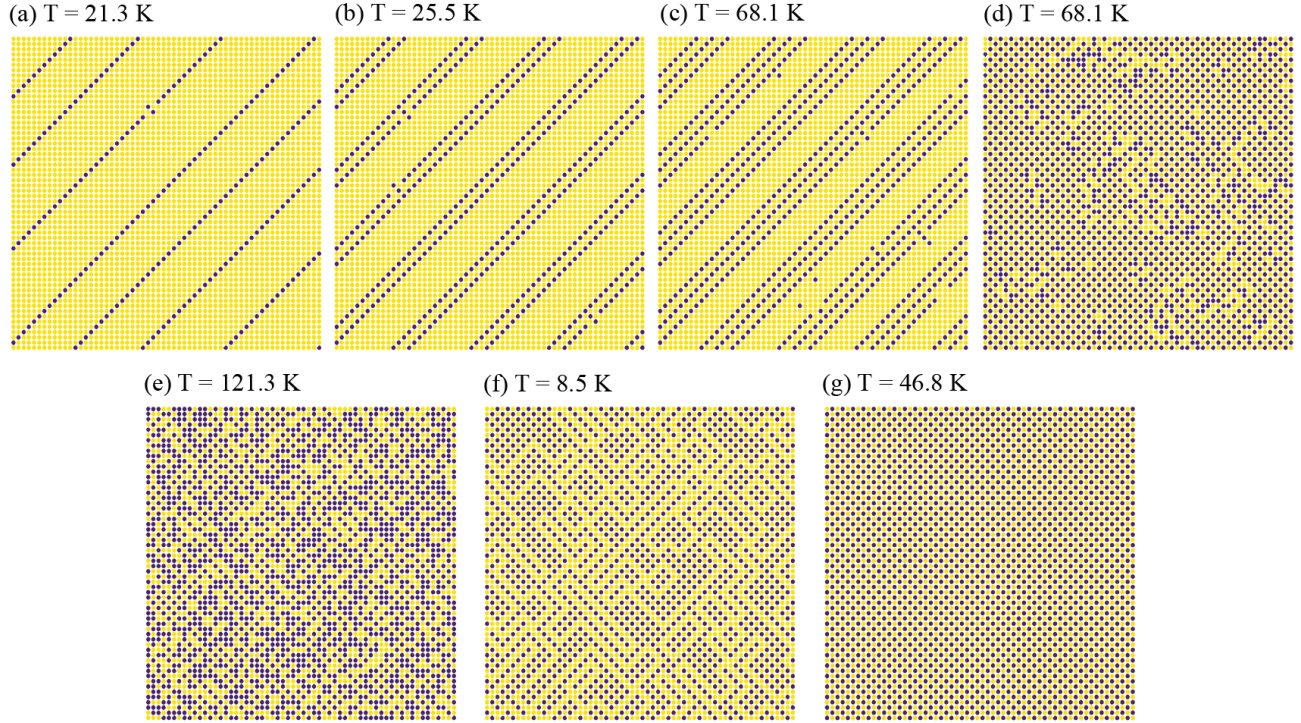


FIG. 7. Snapshots from the Monte Carlo simulation reveal the diversity of spin-state orderings that are possible in this model. Snapshots are of the lattice configurations at selected temperatures for the calculations reported in Fig. 6. Yellow points correspond to LS metals and purple to HS metals.

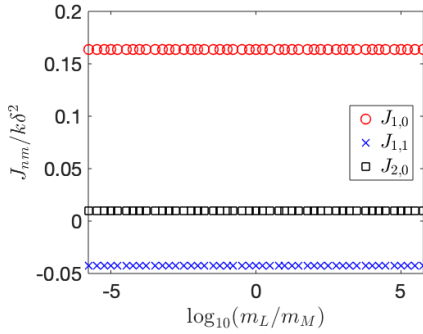


FIG. 8. $J_{1,0}$, $J_{1,1}$, and $J_{2,0}$, calculated using the dynamical matrix basis, as a function of m_L . It can be seen that the Ising coupling constants do not depend on the masses of the ligands and the metals, and are independent on the dynamics of the system. Here $k_\theta = k$, but equivalent results are found for other k_θ/k .

ments, $d_{\nu,\nu',\mathbf{q}}^{\alpha,\alpha'}$, are related to the Hessian by

$$d_{\nu,\nu',\mathbf{q}}^{\alpha,\alpha'} = \frac{\mathbf{f}_{\nu,\nu',\mathbf{q}}^{\alpha,\alpha'}}{\sqrt{m_\nu m_{\nu'}}}. \quad (\text{A3})$$

Using the eigenvectors of $\mathcal{D}_\mathbf{q}$ as our basis we can write

H_u in the form

$$H_u = \frac{1}{2} \sum_{\mu,\mathbf{q}} (P_{\mu,\mathbf{q}} P_{\mu,-\mathbf{q}} + \omega_{\mu,\mathbf{q}}^2 Q'_{\mu,\mathbf{q}} Q'_{\mu,-\mathbf{q}}), \quad (\text{A4})$$

where we identify $Q'_{\mu,\mathbf{q}}$ as the normal coordinate for the collective mode $\mu\mathbf{q}$, μ enumerates the eigenvalues/vectors of $\mathcal{D}_\mathbf{q}$, and

$$P_{\mu,\mathbf{q}} = \dot{Q}'_{\mu,\mathbf{q}}^*, \quad (\text{A5})$$

furthermore, we have

$$H_{u\sigma} = \sum_{\mu,\mathbf{q}} \xi'_\mu(\mathbf{q}) Q'_{\mu,\mathbf{q}} \sigma_{-\mathbf{q}}. \quad (\text{A6})$$

After applying the displaced coordinate transformation, we arrive to the expressions

$$H_v = \frac{1}{2} \sum_{\mu,\mathbf{q}} [P_{\mu,\mathbf{q}} P_{\mu,-\mathbf{q}} + \omega_{\mu,\mathbf{q}}^2 v'_{\mu,\mathbf{q}} v'_{\mu,-\mathbf{q}}] \quad (\text{A7})$$

$$H_{\sigma\sigma} = - \sum_{\mu,\mathbf{q}} \frac{|\xi'_\mu(\mathbf{q})|^2}{2\omega_{\mu,\mathbf{q}}^2} \sigma_\mathbf{q} \sigma_{-\mathbf{q}}. \quad (\text{A8})$$

where as $N \rightarrow \infty$

$$J_n = - \frac{\Omega}{(2\pi)^d} \int_{BZ} d^d \mathbf{q} \sum_{\mu} \frac{|\xi'_\mu(\mathbf{q})|^2}{2\omega_{\mu,\mathbf{q}}^2} e^{i\mathbf{q} \cdot (\mathbf{R}_i - \mathbf{R}_{i+n})}. \quad (\text{A9})$$

We have used two distinct bases, the eigenvectors of the Hessian (Eq. 28) and the eigenvectors of the dynamical matrix (Eq. A9), to yield expressions of J_n . The dynamical matrix basis makes the masses of the ligands and metals appear explicitly on the expression of J_n . However, the two expressions must be equal. Therefore, the Ising coupling constants obtained using the mass dependent basis (dynamical matrix) are equal to the Ising coupling constants obtained with the mass independent basis (Hessian matrix) and the Ising coupling constants do not depend on the masses of the constituents of the system. Similarly, the Ising coupling constants cannot depend on the dynamics of the system. This is confirmed numerically, Fig. 8.

This allows us to write H_v using the dynamical matrix

basis and $H_{\sigma\sigma}$ using the Hessian basis, such that

$$H_v + H_{\sigma\sigma} = \frac{1}{2} \sum_{\mu, \mathbf{q}} [P_{\mu, \mathbf{q}} P_{\mu, -\mathbf{q}} + \omega_{\mu, \mathbf{q}}^2 v'_{\mu, \mathbf{q}} v'_{\mu, -\mathbf{q}}] - \sum_{\mu, \mathbf{q}} \frac{|\xi_{\mu}(\mathbf{q})|^2}{2\kappa_{\mu, \mathbf{q}}} \sigma_{\mathbf{q}} \sigma_{-\mathbf{q}}. \quad (\text{A10})$$

In the context of collective Jahn-Teller transitions in transition metal spinels, Kanamori [50], used displaced operators to transform to new phonon operators. This method yields an expression of the same form as Eq. (A8) [51, 52], where the intermolecular interaction was attributed to the exchange of virtual phonons. In our model this might appear to be also the case, but the Hessian basis shows that the interaction is not dynamical in origin.

As with the calculation of Ising coupling constants from the Hessian matrix, resolving the J_{nm} into the contributions from individual phonons does not provide any clear insight into their origin. In fact, the phonon basis is even worse than the Hessian basis as the contributions of the individual modes (Fig. S3) depend on the masses of the components even though their sum, Fig. 8, does not!

-
- [1] A. Hauser, Ligand field theoretical considerations, in *Spin Crossover in Transition Metal Compounds I. Topics in Current Chemistry*, Vol. 233, edited by P. Gülich and H. Goodwin (Springer, Berlin, Heidelberg, 2004).
- [2] S. Cobo, D. Ostrovskii, S. Bonhommeau, L. Vendier, G. Molnr, L. Salmon, K. Tanaka, and A. Bousseksou, Single-laser-shot-induced complete bidirectional spin transition at room temperature in single crystals of (feii(pyrazine)(pt(cn)4)), *Journal of the American Chemical Society* **130**, 9019 (2008).
- [3] V. Ksenofontov, A. B. Gaspar, and P. Gülich, Pressure effect studies on spin crossover and valence tautomeric systems, in *Spin Crossover in Transition Metal Compounds III* (Springer Berlin Heidelberg, Berlin, Heidelberg, 2004) pp. 23–64.
- [4] A. Bousseksou, F. Varret, M. Goiran, K. Boukheddaden, and J. P. Tuchagues, The spin crossover phenomenon under high magnetic field, in *Spin Crossover in Transition Metal Compounds III* (Springer Berlin Heidelberg, Berlin, Heidelberg, 2004) pp. 65–84.
- [5] F. Prins, M. Monrabal-Capilla, E. A. Osorio, E. Coronado, and H. S. J. van der Zant, Room-temperature electrical addressing of a bistable spin-crossover molecular system, *Advanced Materials* **23**, 1545 (2011).
- [6] J. Pavlik and R. Boa, Established static models of spin crossover, *European Journal of Inorganic Chemistry* **2013**, 697 (2013).
- [7] P. Gülich and H. A. Goodwin, Spin crossover—an overall perspective, in *Spin Crossover in Transition Metal Compounds I*, edited by P. Gülich and H. Goodwin (Springer Berlin Heidelberg, Berlin, Heidelberg, 2004) pp. 1–47.
- [8] A. Bousseksou, G. Molnr, L. Salmon, and W. Nicolazzi, Molecular spin crossover phenomenon: recent achievements and prospects, *Chem. Soc. Rev.* **40**, 3313 (2011).
- [9] P. Guionneau, Crystallography and spin-crossover. a view of breathing materials, *Dalton Trans.* **43**, 382 (2014).
- [10] B. R. Mullaney, L. Goux-Capes, D. J. Price, G. Chastanet, J.-F. Létard, and C. J. Kepert, Spin crossover-induced colossal positive and negative thermal expansion in a nanoporous coordination framework material, *Nature Communications* **8**, 10.1038/s41467-017-00776-1 (2017).
- [11] J. Wajnlasz and R. Pick, Transitions “Low Spin”-“High Spin” Dans les complexes de Fe^{2+} , *Journal de Physique Colloques* **32**, C1 (1971).
- [12] Y. Konishi, H. Tokoro, M. Nishino, and S. Miyashita, Monte carlo simulation of pressure-induced phase transitions in spin-crossover materials, *Phys. Rev. Lett.* **100**, 067206 (2008).
- [13] R. Traiche, M. Sy, and K. Boukheddaden, Elastic frustration in 1d spin-crossover chains: Evidence of multi-step transitions and self-organizations of the spin states, *The Journal of Physical Chemistry C* **122**, 4083 (2018).
- [14] M. Nishino, K. Boukheddaden, Y. Konishi, and S. Miyashita, Simple two-dimensional model for the elastic origin of cooperativity among spin states of spin-crossover complexes, *Phys. Rev. Lett.* **98**, 247203 (2007).
- [15] M. Nishino, K. Boukheddaden, and S. Miyashita, Molecular dynamics study of thermal expansion and compression in spin-crossover solids using a microscopic model of elastic interactions, *Phys. Rev. B* **79**, 012409 (2009).
- [16] C. Enachescu, M. Nishino, S. Miyashita, L. Stoleriu, and A. Stancu, Monte carlo metropolis study of cluster evo-

- lution in spin-crossover solids within the framework of a mechanoelastic model, *Phys. Rev. B* **86**, 054114 (2012).
- [17] M. Paez-Espejo, M. Sy, and K. Boukheddaden, Elastic frustration causing two-step and multistep transitions in spin-crossover solids: Emergence of complex antiferroelastic structures, *Journal of the American Chemical Society* **138**, 3202 (2016).
- [18] N. Ortega-Villar, M. Muoz, and J. Real, Symmetry breaking in iron(II) spin-crossover molecular crystals, *Magnetochemistry* **2**, 16 (2016).
- [19] J. Cruddas and B. J. Powell, Structure-property relationships and the mechanisms of multistep transitions in spin crossover materials and frameworks, arXiv:2006.03255 (2020).
- [20] G. J. Halder, C. J. Kepert, B. Moubaraki, K. S. Murray, and J. D. Cashion, Guest-dependent spin crossover in a nanoporous molecular framework material, *Science* **298**, 1762 (2002).
- [21] Z.-P. Ni, J.-L. Liu, M. N. Hoque, W. Liu, J.-Y. Li, Y.-C. Chen, and M.-L. Tong, Recent advances in guest effects on spin-crossover behavior in hofmann-type metal-organic frameworks, *Coordination Chemistry Reviews* **335**, 28 (2017).
- [22] K. Boukheddaden, S. Miyashita, and M. Nishino, Elastic interaction among transition metals in one-dimensional spin-crossover solids, *Phys. Rev. B* **75**, 094112 (2007).
- [23] H. J. Monkhorst and J. D. Pack, Special points for brillouin-zone integrations, *Phys. Rev. B* **13**, 5188 (1976).
- [24] C. J. Adams, M. C. Muñoz, R. E. Waddington, and J. A. Real, Cooperative Spin Transition in the Two-Dimensional Coordination Polymer $[\text{Fe}(4,4'\text{-bipyridine})_2(\text{NCX})_2] \cdot 4\text{CHCl}_3$ $X = \text{S}, \text{Se}$, *Inorg. Chem.* **50**, 10633 (2011).
- [25] J.-B. Lin, W. Xue, B.-Y. Wang, J. Tao, W.-X. Zhang, J.-P. Zhang, and X.-M. Chen, Chemical/physical pressure tunable spin-transition temperature and hysteresis in a two-step spin crossover porous coordination framework, *Inorg. Chem.* **51**, 9423 (2012).
- [26] X. Bao, P.-H. Guo, W. Liu, J. Tucek, W.-X. Zhang, J.-D. Leng, X.-M. Chen, I. A. Gural'skiy, L. Salmon, A. Bousseksou, and M.-L. Tong, Remarkably high-temperature spin transition exhibited by new 2D metal-organic frameworks, *Chem. Sci.* **3**, 1629 (2012).
- [27] G. J. Halder, K. W. Chapman, S. M. Neville, B. Moubaraki, K. S. Murray, J.-F. Létard, and C. J. Kepert, Elucidating the mechanism of a two-step spin transition in a nanoporous metal-organic framework, *J. Am. Chem. Soc.* **130**, 17552 (2008).
- [28] J. E. Clements, J. R. Price, S. M. Neville, and C. J. Kepert, Hysteretic four-step spin crossover within a three-dimensional porous hofmann-like material, *Angewandte Chemie International Edition* **55**, 15105 (2016).
- [29] C.-J. Zhang, K.-T. Lian, G.-Z. Huang, S. Bala, Z.-P. Ni, and M.-L. Tong, Hysteretic four-step spin-crossover in a 3D hofmann-type metalorganic framework with aromatic guest, *Chem. Commun.* **55**, 11033 (2019).
- [30] G. Agustí, M. C. Muñoz, A. B. Gaspar, and J. A. Real, Spin-crossover behavior in cyanide-bridged iron(II)-gold(I) bimetallic 2D hofmann-like metal-organic frameworks, *Inorg. Chem.* **47**, 2552 (2008).
- [31] C.-J. Zhang, K.-T. Lian, S.-G. Wu, G.-Z. Huang, Z.-P. Ni, and M.-L. Tong, The substituent guest effect on four-step spin-crossover behaviors, *Inorg. Chem. Front.* **4**, 911 (2020).
- [32] W. Liu, Y.-Y. Peng, S.-G. Wu, Y.-C. Chen, M. N. Hoque, Z.-P. Ni, X.-M. Chen, and M.-L. Tong, Guest-switchable multi-step spin transitions in an amine-functionalized metalorganic framework, *Angew. Chem. Int. Ed.* **56**, 14982 (2017).
- [33] G. Agustí, A. B. Gaspar, M. C. Muñoz, P. G. Lacroix, and J. A. Real, Spin crossover and paramagnetic behaviour in two-dimensional iron(II) coordination polymers with stilbazole pushpull ligands, *Aust. J. Chem.* **62**, 1155 (2009).
- [34] K. Takashi, K.-T. Chihiro, K. Chikahide, S. Toshiaki, and K. Takafumi, Isotope effect on spin-crossover transition in a new two-dimensional coordination polymer $[\text{FeII}(\text{C}_5\text{H}_5\text{N})_2][\text{AuI}(\text{CN})_2]_2$, $[\text{FeII}(\text{C}_5\text{D}_5\text{N})_2][\text{AuI}(\text{CN})_2]_2$, and $[\text{FeII}(\text{C}_5\text{H}_5\text{N})_2][\text{AuI}(\text{CN})_2]_2$, *Chem. Lett.* **37**, 422 (2008).
- [35] Y. Meng, Q. Sheng, M. N. Hoque, Y. Chen, S. Wu, J. Tucek, R. Zboril, T. Liu, Z. Ni, and M. Tong, Two-step spin-crossover with three inequivalent Fe^{II} sites in a two-dimensional hofmann-type coordination polymer, *Chem. Eur. J.* **23**, 10034 (2017).
- [36] T. Nakada, P. A. Rikvold, T. Mori, M. Nishino, and S. Miyashita, Crossover between a short-range and a long-range ising model, *Phys. Rev. B* **84**, 054433 (2011).
- [37] T. Nakada, T. Mori, S. Miyashita, M. Nishino, S. Todo, W. Nicolazzi, and P. A. Rikvold, Critical temperature and correlation length of an elastic interaction model for spin-crossover materials, *Phys. Rev. B* **85**, 054408 (2012).
- [38] S. Miyashita, Y. Konishi, M. Nishino, H. Tokoro, and P. A. Rikvold, Realization of the mean-field universality class in spin-crossover materials, *Phys. Rev. B* **77**, 014105 (2008).
- [39] J. Cruddas and B. J. Powell, Spin-state ice in elastically frustrated spin-crossover materials, *Journal of the American Chemical Society* **141**, 19790 (2019).
- [40] J. Cruddas and B. J. Powell, Multiple Coulomb phases with temperature tunable ice rules in pyrochlore spin crossover materials, arXiv:2007.13983 (2020).
- [41] C. Castelnovo, R. Moessner, and S. Sondhi, Spin ice, fractionalization, and topological order, *Annu. Rev. Condens. Matter Phys.* **3**, 35 (2012).
- [42] H.-Z. Ye, C. Sun, and H. Jiang, Monte-carlo simulations of spin-crossover phenomena based on a vibronic ising-like model with realistic parameters, *Phys. Chem. Chem. Phys.* **17**, 6801 (2015).
- [43] J. C. Tan and A. K. Cheetham, Mechanical properties of hybrid inorganicorganic framework materials: establishing fundamental structure-property relationships, *Chem. Soc. Rev.* **40**, 1059 (2011).
- [44] E. C. Spencer, R. J. Angel, N. L. Ross, B. E. Hanson, and J. A. K. Howard, Pressure-induced cooperative bond rearrangement in a zinc imidazolate framework: A high-pressure single-crystal x-ray diffraction study, *Journal of the American Chemical Society* **131**, 4022 (2009).
- [45] M. Mikolasek, M. D. Manrique-Juarez, H. J. Shepherd, K. Ridier, S. Rat, V. Shalabaeva, A.-C. Bas, I. E. Collings, F. Mathieu, J. Cacheux, T. Leichle, L. Nicu, W. Nicolazzi, L. Salmon, G. Molnr, and A. Bousseksou, Complete set of elastic moduli of a spin-crossover solid: Spin-state dependence and mechanical actuation, *Journal of the American Chemical Society* **140**, 8970 (2018).
- [46] D. J. Harding, P. Harding, and W. Phonsri, Spin crossover in iron(iii) complexes, *Coordination Chemistry Reviews* **313**, 38 (2016).

- [47] C. P. Slichter and H. G. Drickamer, Pressureinduced electronic changes in compounds of iron, *The Journal of Chemical Physics* **56**, 2142 (1972).
- [48] O. Roubeau, M. Castro, R. Burriel, J. G. Haasnoot, and J. Reedijk, Calorimetric investigation of triazole-bridged fe(ii) spin-crossover one-dimensional materials: Measuring the cooperativity, *The Journal of Physical Chemistry B* **115**, 3003 (2011), pMID: 21381636.
- [49] Y.-Y. Peng, S.-G. Wu, Y.-C. Chen, W. Liu, G.-Z. Huang, Z.-P. Ni, and M.-L. Tong, Asymmetric seven-/eight-step spin-crossover in a three-dimensional hofmann-type metalorganic framework, *Inorg. Chem. Front.* **7**, 1685 (2020).
- [50] J. Kanamori, Crystal distortion in magnetic compounds, *Journal of Applied Physics* **31**, S14 (1960).
- [51] G. A. Gehring and K. A. Gehring, Co-operative jahn-teller effects, *Reports on Progress in Physics* **38**, 1 (1975).
- [52] T. Kambara, Theory of highspin lowspin transitions in transition metal compounds induced by cooperative molecular distortions and lattice strains, *The Journal of Chemical Physics* **74**, 4557 (1981).

Supplementary material for “Equivalence of elastic and Ising models for spin crossover materials”

Gian Ruzzi, Jace Cruddas, Ross H. McKenzie, and Ben J. Powell
 School of Mathematics and Physics, The University of Queensland, QLD 4071, Australia

I. SHEAR MODULUS

The shear modulus is defined as

$$G = \frac{F/A}{\Delta x/l} \quad (\text{S1})$$

where F is a force applied on a surface A leading to an angular displacement γ such that $\tan \gamma = \Delta x/l$ as indicated in Fig. S1. For small γ we can make the approximation $\tan \gamma \approx \gamma$, and we let $r_o = \bar{R} + \delta\langle\sigma\rangle$ be the distance between a metal and ligand, therefore

$$G = \frac{F}{\gamma A} \quad (\text{S2})$$

The force F at mechanical equilibrium is equal in magnitude and opposite in direction to the x component of the force on a single layer from all other particles in the system. We assume that none of the springs are either stretched or compressed, such that there are no contributions to the force due to stretching. Now consider a metal site and its six nearest ligands, a strain will lead to an angle dependent force on metal M , but the only particles involved are those in the $x - y$ plane, see Fig. S1, because the angle between the other bonds is $\pi/2$. From our Hamiltonian [Eq. (1)], the energy contribution due to angle θ_{ijk} between the bonds formed

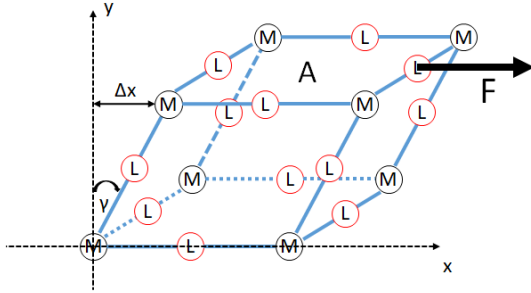


FIG. S1. Shear strain on a unit cell of a cubic lattice with the arrangement of ligands (L) and metals (M) described in the paper. A is the area a single layer, F is an externally applied force, Δx is the displacement of the layer from the y axis, γ is the angular displacement due to force F .

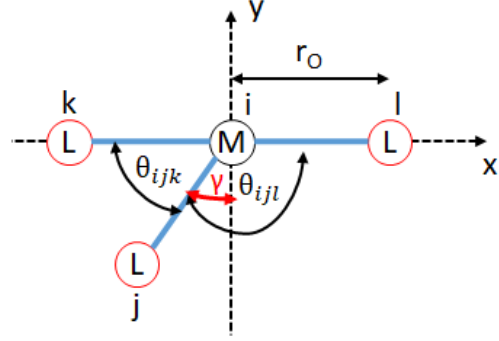


FIG. S2. Schematic of a single metal site in the top layer of a cubic lattice.

by $M_i - L_j$ and $M_i - L_k$, see Fig. S2, is given by

$$V(\theta_{ijk}) = \bar{R}^2 \frac{k_\theta}{2} \sin^2 \left(\theta_{ijk} - \frac{\pi}{2} \right). \quad (\text{S3})$$

In general

$$\cos \theta_{ijk} = \frac{(\mathbf{r}_k - \mathbf{r}_i) \cdot (\mathbf{r}_j - \mathbf{r}_i)}{|\mathbf{r}_k - \mathbf{r}_i| |\mathbf{r}_j - \mathbf{r}_i|} = \frac{(\mathbf{r}_k - \mathbf{r}_i) \cdot (\mathbf{r}_j - \mathbf{r}_i)}{r_o^2}, \quad (\text{S4})$$

where r_o is the equilibrium spacing between a metal and the ligands it is covalently bound to, and, for small γ ,

$$\cos \theta_{ijk} = \cos \left(\frac{\pi}{2} - \gamma \right) = \sin \gamma \approx \gamma = \frac{\pi}{2} - \theta_{ijk}. \quad (\text{S5})$$

Therefore,

$$\frac{\partial \theta_{ijk}}{\partial \mathbf{r}_i} = \frac{\mathbf{r}_{ji} + \mathbf{r}_{ki}}{r_o^2} = -\frac{\hat{\mathbf{x}}(1 + \sin \gamma) + \hat{\mathbf{y}} \cos \gamma}{r_o} \quad (\text{S6})$$

and the force on metal i due to ligands j and k is

$$\begin{aligned} \mathbf{f}_{i;jk} &= -\frac{\partial V}{\partial \theta_{ijk}} \frac{\partial \theta_{ijk}}{\partial \mathbf{r}_i} \\ &= -\frac{\bar{R}^2 k_\theta \gamma (1 + \sin \gamma)}{r_o} \hat{\mathbf{x}} - \frac{\bar{R}^2 k_\theta \gamma \cos \gamma}{r_o} \hat{\mathbf{y}} \end{aligned} \quad (\text{S7})$$

Following the same procedure for the angle θ_{ijl} , see Fig. S2, yields

$$\mathbf{f}_{i;jl} = -\frac{\bar{R}^2 k_\theta \gamma (1 - \sin \gamma)}{r_o} \hat{\mathbf{x}} + \frac{\bar{R}^2 k_\theta \gamma \cos \gamma}{r_o} \hat{\mathbf{y}}. \quad (\text{S8})$$

Hence the total force on metal i due to displacement γ is

$$\mathbf{f}_i = -\frac{2\bar{R}^2 k_\theta \gamma}{r_o} \hat{\mathbf{x}}. \quad (\text{S9})$$

A single layer of a cubic system has $N^{2/3}$ metals, where N is the total number of metals. Therefore, the force applied on the system is $\mathbf{F} = -N^{2/3} \mathbf{f}_i$. The surface area of a single layer is $A = N^{2/3} 4r_o^2$ therefore $G = \bar{R}^2 k_\theta / 2r_o^3$. For $\delta \ll \bar{R}$ we can approximate $r_o = \bar{R} + \delta \langle \sigma \rangle \approx \bar{R}$, and hence

$$G = \frac{k_\theta}{2\bar{R}}. \quad (\text{S10})$$

If the shear modulus has not been directly measured it can be calculated from Young's modulus Y , bulk modulus B , and Poisson's ratio ν [1] via

$$G = \frac{3BY}{9B - Y}, \quad (\text{S11})$$

$$G = \frac{Y}{2(1 + \nu)}. \quad (\text{S12})$$

II. DECOMPOSITION OF THE ISING COUPLING CONSTANTS

The contributions from the different $J_{n,m}^\mu$ change as the ratio k_θ/k changes, Figs. S3a to S3c. The contributions from $\mu = 4, 5, 6$ decrease as k_θ/k increases. This is because $J_{n,m}^\mu$ is inversely proportional to $\kappa_{\mu,q}$, [Eq. (29)], and, for large k_θ/k , the magnitudes of $\kappa_{\mu,q}$ for $\mu = 4, 5, 6$ are much larger than for $\mu = 1, 2, 3$, Figs. S3d to S3f. There is also a subtle competition between the different $J_{n,m}^\mu$, as their signs alternate and their magnitudes differ from each other. For the three cases considered, the magnitudes and signs of $J_{n,m}^\mu$ change drastically as k_θ/k varies, where some $J_{n,m}^\mu$ can become considerably larger in magnitude than the others, but their signs alternate which makes the resultant Ising coupling constants smaller.

When written in the phononic basis (see Appendix) the contributions to J_{nm} from individual modes depends on the ratio of masses, even though their sum does not.

[1] L. D. Landau and E. M. Lifshits, *Theory of elasticity*, 2nd ed., Course of theoretical physics ; v. 7 (Pergamon Press, Oxford ; New York, 1970).

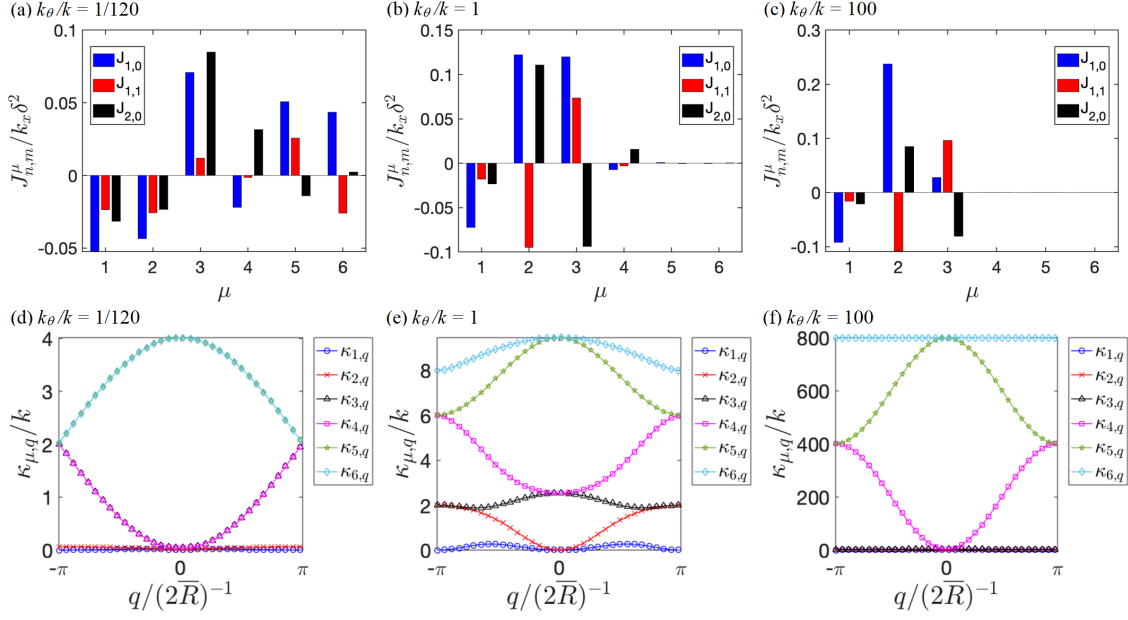


FIG. S3. (a-c) The contributions to $J_{1,0}$, $J_{1,1}$, and $J_{2,0}$ from the different eigenvalues/eigenvectors of the Hessian matrix, [Eq. (28)], are shown for different k_{θ}/k . (d-f) Eigenvalues of the Hessian matrix, $\kappa_{\mu,q}$, as a function of q along $q = q_x = q_y$, for different values of k_{θ}/k . For large k_{θ}/k , the dominant contributions come from $\mu = 1, 2, 3$; this is because of the large magnitudes of eigenvalues $\mu = 3, 4, 5$, as shown in the bottom plots; and because $J_{n,m}^{\mu}$ is inversely proportional to the eigenvalues of the Hessian matrix, [Eq. (29)]. Here, we can also see the subtle competition between the different contributions, and how their relative signs stop changing for large k_{θ} .

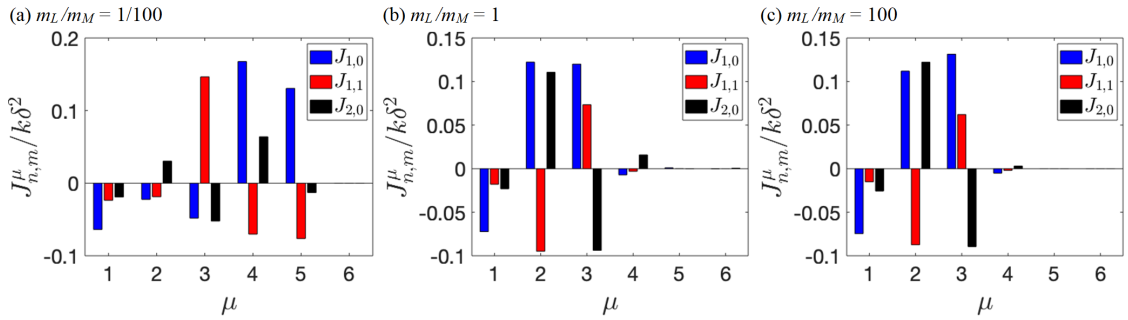


FIG. S4. The contributions to $J_{1,0}$, $J_{1,1}$, and $J_{2,0}$ from the different eigenvalues/eigenvectors of the dynamical matrix, see Eq. (A9) [cf. Eq. (28)], for different values of m_L/m_M for $m_{L1} = m_{L2} = m_L$. The contributions change as the mass changes, where for large m_L/m_M the main contributions come from $\mu = 1, 2, 3$. In all plots, $k_{\theta} = k$.